Pacific Northwest NATIONAL LABORATORY

PNNL-34995

Sensing and Control During Bulk SPP

September 2023

Julian D Escobar
Brandon S Taysom
Glenn J Grant
Scott A Whalen

U.S. DEPARTMENT OF ENERGY

Prepared for the U.S. Department of Energy
under Contract DE-AC05-76RL01830

PACIFIC NORTHWEST NATIONAL LABORATORY
operated by
BATTELLE
for the
UNITED STATES DEPARTMENT OF ENERGY
under Contract DE-AC05-76RL01830

Printed in the United States of America

Available to DOE and DOE contractors from
the Office of Scientific and Technical Information,
P.O. Box 62, Oak Ridge, TN 37831-0062
www.osti.gov
ph: (865) 576-8401
fox: (865) 576-5728
email: reports@osti.gov

Available to the public from the National Technical Information Service
5301 Shawnee Rd., Alexandria, VA 22312
ph: (800) 553-NTIS (6847)
or (703) 605-6000
email: info@ntis.gov
Online ordering: http://www.ntis.gov

PNNL-34995

Sensing and Control During Bulk SPP

September 2023

Julian D Escobar
Brandon S Taysom
Glenn J Grant
Scott A Whalen

Prepared for
the U.S. Department of Energy
under Contract DE-AC05-76RL01830

Pacific Northwest National Laboratory
Richland, Washington 99354

Abstract

In this work, we use the thermoelectricity to directly measure the temperature at different radial positions within instrumented Al1100 billets during friction extrusion. Site-specific and uninterrupted temperature measurements were possible by measuring the local voltages at several thermoelectric junctions consisting of aluminum-nickel pairs during extrusion. Measurements were conducted for a constant die rotation speed of 150 RPM and different extrusion feed rates of 2, 8, 32, and 80 mm.min-1. X-ray computed tomography was used to locate the positions of the thermoelectric junctions inside the processed billet, thus allowing for site-specific microstructural characterization at the precise measurement points. Smooth particle hydrodynamic modeling allowed to determine the thermal, strain, and strain rate fields developing during FE. The applicability and limitations of this temperature measurement approach are discussed as a function of the peak extrusion and torsion stresses relative to the matrix of extrusion feed rates.

Summary

During friction extrusion the deforming microstructure cannot be directly probed with conventional contact thermocouples or non-contact infrared-based techniques since the plasticized metal is confined inside a container or is passing through an extrusion die. In this work, we demonstrate for the first time the use of the thermoelectric effect to locally measure the temperature profiles inside an extruding Al billet at different radial position and probing depths. A series of enamel coated Ni wires positioned inside the Al billet are used as site-specific probes, capable of measuring local thermoelectric voltages developing upon friction extrusion. Internal temperature measurements were conducted for a constant die rotation speed of 150 RPM and varying extrusion feed rates of 2, 8, 32, and 80 mm.min-1, which led to peak extrusion pressures of 216, 206, 373 and 473 MPa, and peak torsion stresses of 79, 59, 108 and 147 MPa, respectively. X-ray computed tomography, electron backscatter diffraction and smooth particle hydrodynamic modeling were used to understand the correlation between temperature and local microstructural evolution at the points of thermoelectric contact. Our results show that electric potentials can be measured at the thermoelectric junctions inside the deformation zone even during the continuous process of Ni wire tip fracture and co-extrusion as the billet is consumed. Upon fracture, Ni fragments are immediate disconnection from the circuit, but an uninterrupted measurement is guaranteed via in situ generation of fresh thermoelectric junctions at the new points of contact. The applicability and limitations of this temperature measurement approach are discussed.

Acknowledgments

This research was supported by the **Solid Phase Processing Science Initiative,** under the Laboratory Directed Research and Development (LDRD) Program at Pacific Northwest National Laboratory (PNNL). PNNL is a multi-program national laboratory operated for the U.S. Department of Energy (DOE) by Battelle Memorial Institute under Contract No. DE-AC05-76RL01830.

Acronyms and Abbreviations

DRX: dynamic recrystallization

FE: friction extrusion

ShAPE: shear assisted processing and extrusion

SPP: solid phase processing

TE: thermoelectricity

Contents

Figures

Tables

1.0 Introduction

Friction extrusion (FE) is a solid phase processing (SPP) method, which uses a rotational hollow die and a stationary feedstock container (with either a solid billet or particulated material) to generate an extrudate via the combination of frictional and deformation heating, axial extrusion force, and torque [1-4]. This process shares multiple similarities with the plunging stage during friciton stir processing (FSP), or with friction stir backing extrusion (FSBE) [5], where a rotating tool applies a compressive force and torque to progressively heat and stir a volume of material without translational motion. However, during FE, the plasticized region generated underneath the die/billet interface is rather forced along the hollow die, forming a rod-shaped final product. The use of FE as an advanced metal manufactuirng technique offers a series of advantages relative to conventional direct extrusion, such as enhanced extrudability [2, 6, 7], and the hability to produce bulk pieces from pusupecursor powders via friciton alloying [1, 2, 8, 9]. Materials processing via FE opens the door to ultra-fast microstructural and alloy design. However, in order to harvest the potential of FE for such applications, one of the most pressing issues that needs to be addressed is temperature control.

Conventionally, temperature measurements during SPP are challenging. The inhability to directly probe the deforming microstructure is a well-known issue within the FSP community [10-13]. Typically, contact thermocouples are placed at the vicinities of the stir zone [11, 14] and therefore the measured thermal cycles are not representative of the processing microstructure. Thermocouples can also be inserted in the processing tool during FSP [15, 16], but it should be taken into account that the temperature measurement is more closely related to the response of the tool material mediated by its particular thermal conductivity. A similar approach is used during conventional FS, where the rotating die is instrumented with a conventional contact thermocouple near (but not at) the die/billet interface [1, 6, 7]. Other non-contact techniques, such as infrared cameras using transparent yttrium aluminum garnet (YAG) windows, have been used to monitor the temperature of deforming metals during machining operations [17]. However, YAG windows are brittle and can crack during FSP or FE operations.

An alternative method to study the temperature cycles inside deforming microstructures during SPP is based on the thermoelectric effect (TE). This method consists of the measurement of the electric potential that appears in metals upon a temperature gradient. Different metals have specific responses to the TE effect and are well represented by the Seebeck coefficient [18]. This is the principle upon which contact thermocouples operate, where large differences between Seebeck coefficients of two metals are desired to increase the measurement accuracy. Temperature measurements using the TE effect were performed by Backer, et. al [10] and Silva-Magalhaes, et al., [16] during FSP experiments. The thermoelectric potential between a reference cold junction and the steel tool – Al workpiece contact interface was retrieved and transformed into temperature. This method is especially useful during the early process of plunging, when conventional thermocouples located at the tool shoulder are not in contact with the workpiece. Recently, Taysom et al. [19], demonstrated the use of the TE effect to precisely measure the temperature right at the interface of a dissimilar Cu/Ni friction weld. It is worth noticing that in all cases [10, 16, 19], the temperature read was related to the average of the contact area between two materials.

2.0 Methodology

In this work, A1100 billets were used to conduct FE experiments using the shear-assisted processing and extrusion (ShAPE) machine at the Pacific Northwest National Laboratory. Differnt extrusion feed rates of 2, 8, 32, and 80 mm.min-1 under a fixed die rotation speed of 150 RPM were studied. In all cases, FS was interrupted at a maximum plunging depth of 20 mm (~ 50% of the billet lenght) to allow further microstructural characterization in the remaining half of the billet.

Figure 1 a) shows the experimental set up inside the ShAPE machine, consisting of a rotating hollow die (left) and a stationary container (right) which holds a bulk Al1100 billet. Figure 1 b) details the experimental configuration during FE, where the rotating die is rammed against the billet, generating a plasticized region at the die/billet interface. The combined action of die rotational speed, extrusion force and torque, and extrusion feed rate, allow for mass transport of plasticized material through the hollow die. Figure 1 c) shows a detail view of the H13 tool steel extrusion die with external and internal diameters of XX mm , XX mm, respectively. The extrusion die consisted of four XX scrolls designed to direct the plasticized material towards a circular throat containing the extrusion hole. Figure 1 d) depicts the cylindrical Al 1100 billet with 31.62 mm in diameter, and 38.1 mm in length. Billets were modified to allow for the insertion of Ni wires along different radial positions and plunging depths. Five holes of 6.35 mm in diameter, namely aluminium Al(1), and nickel Ni(2), Ni(3), Ni(4) and Ni(5) were drilled. The central wire, i.e., Ni(3), was set at the plane of extrusion (0 radius). The relative distances from Ni (3) to Al (1), and Ni (2), Ni (4) and Ni (5), as well as the initial and final positions of the Al/Ni junctions are sumamrized in Table 1.

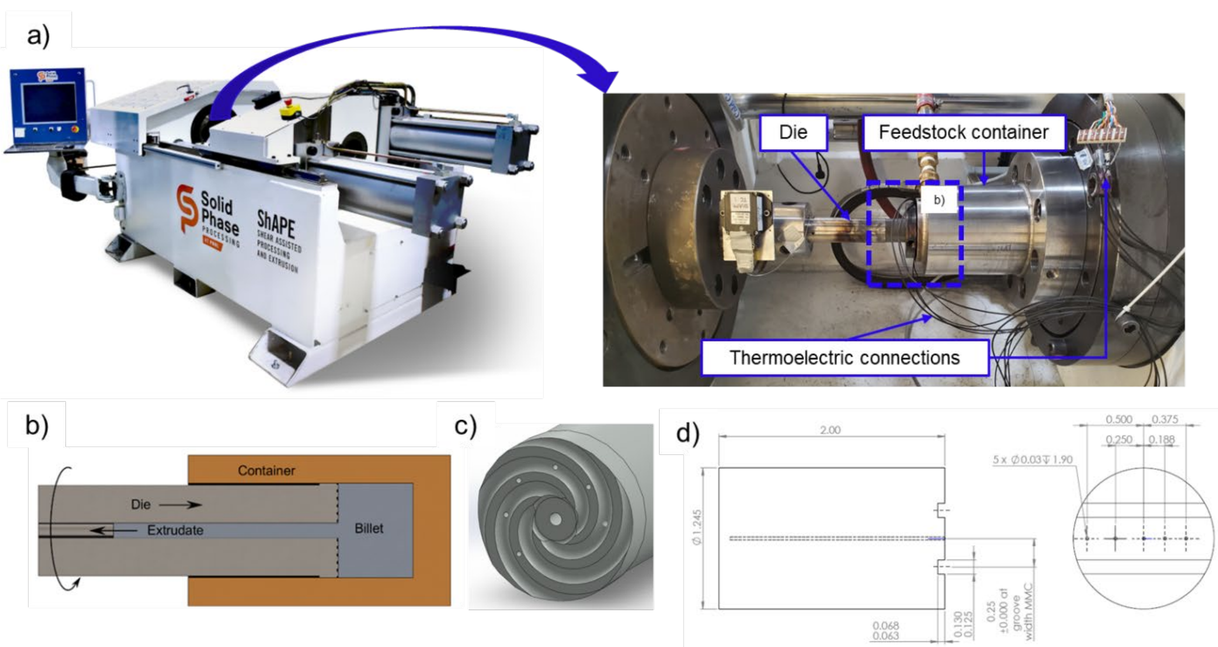

Figure 1. Experimental approach used during thermoelectric voltage measurements during friction extrusion of instrumented Al1100 billets: a) ShAPE machine and detail of the experimental chamber, showing the extrusion die, feedstock container, and thermoelectric connections; b) schematic representation of the die, billet, container and billet; c) rendered image of the extrusion die; d) design of an instrumented Al billet suitable for thermoelectric measurements.

Table 1. Initial and final positions of the Al/Ni thermoelectric junctions along the radial and depth directions. Probing depths are measured from bottom to top and from the top to bottom of the billet (values in parenthesis) before FE, and only from top to bottom after interrupted FE.

TE junction	Initial radial position (mm)	Final radial position (mm)	Initial probing depth (mm)	Final probing depth (mm)
Ni (1)	12.7	12.4	35.6 (2.5)	(6.6)
Ni (2)	6.4	2.2	35.6 (2.5)	(7.3)
Ni (3)	0	0	35.6 (2.5)	(3.6)
Ni (4)	4.6	3.4	35.6 (2.5)	(8.7)
Al (5)	35.6	-	35.6 (2.5)	-

Al-Ni thermoelectric juntions were selected in order to guarantee a sufficiently large voltage signal. The room temperature Seebeck coefficeint for Al and Ni are -1.66 and 19.5 μV/K, respectively, leading to a net difference of 17.8 μV/K [20]. Based on thermoelectricity concepts, the Al1100 billet itself can be understood as half of the thermocouple pair system, with the Al (1) wire serving merely as an electrical connection (positive side) to the TE circuit. On the other hand, the Ni wires (negative side) are used as local probes to measure the electric potential at the points of contact (from now on generically defined as Al/Ni TE junctions). A schematic representation of the Al billet instrumented with one Al wire and several Ni wires is shown Figure 2 a). A detail of the wire insulation process is shown in Figure 2 b). All wires are connected to reference cold junctions (previously calibrated by an ice bath), depicted in Figure 2 c). Additional thermal measurements were collected using a conventional contact thermocouple located near the billet/die interface at approximately 10 mm from the extrusion hole in the radial direction.

Proper electric insulation is imperative for the accuracy of electric potential measurements at the Al/Ni TE junctions. The process of wire insertion and setup assembly is summarized in Figure 2 d). The critical insulation stages are described as follows:

- Enamel coating for Ni wires inside the Al billet:

Before insertion, all Ni wires are electrically insulated with a ~100 μm vitreous enamel coating, (Figure 2 b). This is useful to limit the TE measurement to a single point of contact, which is defined by the interface between the exposed bare Ni wire cross section and the Al billet. The enamel coating also helps to avoid undesired electric contact between Ni wires in case of bending or twisting inside the billet during FE. Note that fractured pieces of Ni wires are immediately disconnected from the circuit, and subsequently extruded. Electric potential measurements will resume at the freshly generated cross section fracture, guaranteeing a continuous voltage read during FE.

- Shapal ceramic base:

A thermally conductive but electrically insulating shapal ceramic base is used to further insulate the base of the billet from the steel feedstock backing, while keeping the Ni wires separated.

- Fiber glass coating for Ni wires outside of the Al billet:

Fiber glass is used as a second insulating barrier for the protruding enamel coated Ni and the bare Al wire. This is useful to prevent further undesired contact between wires and other metallic parts inside the extrusion chamber.

- Silicon nitride (SiN) extrusion container:

The final stage is to replace the extrusion container, typically made of H13 steel, with a thermally conductive but electrically insulating SiN liner. This is important to insulate the whole TE setup from the ShAPE machine.

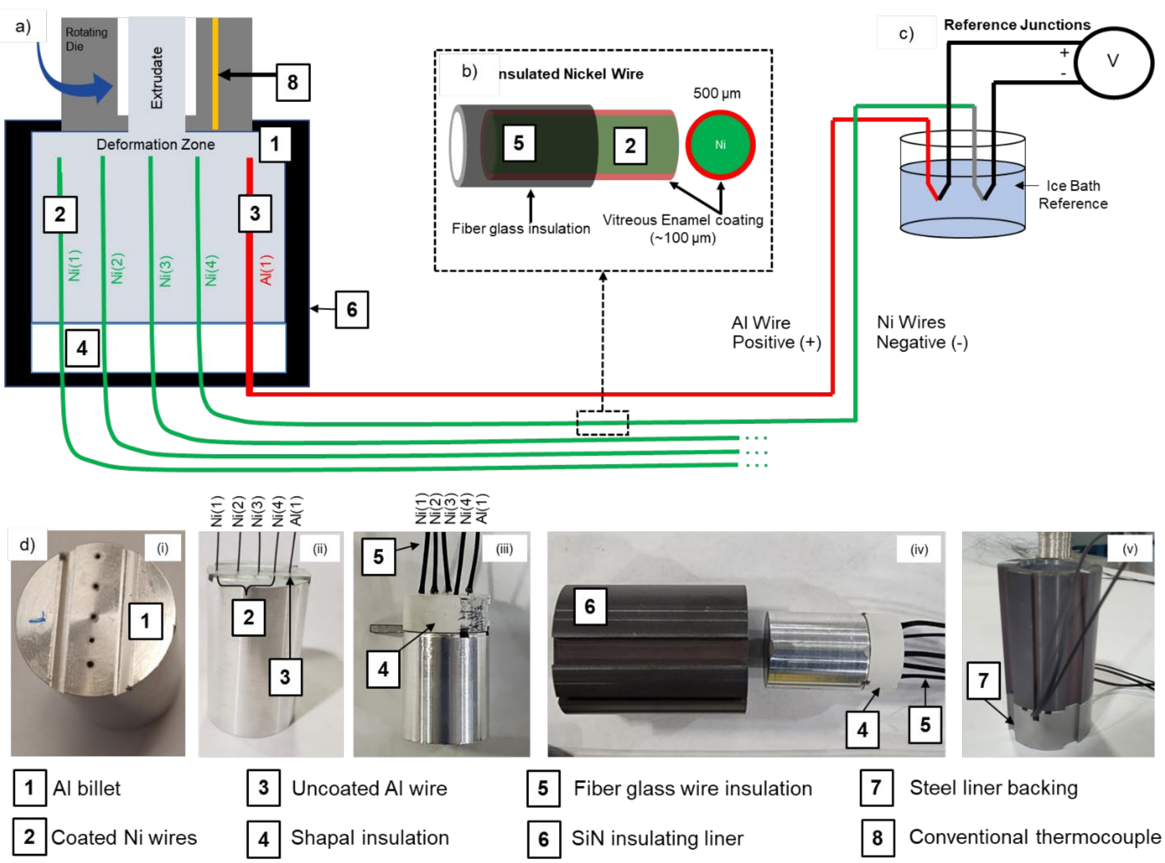

Figure 2. Schematic representation of the thermoelectric measurement set-up used during friction extrusion of Al1100 instrumented billets: a) Al 1100 billet containing multiple Ni wires (negative side) and one Al wire (positive side); b) detail of the insulated Ni wires showing the vitreous enamel coating for insulation inside the billet and and additional fiber glass insulation for all wires protruding from the Al billet. c) reference junction calibrated using an ice bath; d) description of the steps involved in the process of Al billet instrumentation: (i) empty Al billet, (ii) insertion of Ni and Al wires, (iii) setup of insulating shapal ceramic backing and fiber glass wire insulation, (iv) setup of SiN insulating liner, (v) final TE setup.

Partially extruded Al billets (~50 %) were analyzed via X-ray computed tomography to determine the X, Y, and Z coordinates of the final TE junction positions. A Nikon X-Tek/Metris XTH 320/225 kV scanner was set to 95 kV and 280 µA X-ray power, while a 0.5-mm thick Cu filter was used to enhance image contrast by blocking out low-energy x-rays. The billet was rotated continuously during the scans with momentary stops to collect each projection (shuttling mode) while minimizing artifacts. A total of 3142 projections were collected over 360˚ rotation, recording 2 frames per projection, with 500 ms exposure time per frame. The image voxel size was 0.0172 mm. The images were reconstructed to obtain 3D volume data using CT Pro 3D version XT 2.2. After acquiring the XMT images, quantitative analysis was performed using Thermo Fisher Scientific Avizo 9.5.0. We used an interactive thresholding module in Avizo to segment the Al billet and Ni wires.

A JEOL 7600 scanning electron microscope was used to perform EBSD analysis of the transverse section planes of the microstructures at the vicinities of the final Al/Ni TE junctions. An acceleration voltage of 20 keV and a step size of 2 µm were used to characterize the microstructures at the transverse plane that exposed the Ni (3) central and Ni(2) side wires. Additionally, a JEOL 800 scanning electron microscope was used to perform a detailed microstructural evolution characterization through a large montage area, consisting of 124 panels (400 µm wide by 3.04 mm length) to study the microstructural evolution from BM to processed zone. An acceleration voltage of 20 keV and a step size of 500 nm were used.

Data analysis was performed using the MTEX 5.8.2 toolbox [21] in Matlab R2022b. Grain reconstructions were performed for a minimum misorientation threshold of $\omega = 2°$. Low angle grain boundaries (LAGBs) were defined for a $\omega < 15°$ condition, while high angle grain boundaries (HAGBs) were reconstructed for a $\omega \geq 15°$ case [22, 23]. A 5-neighbor pixel cleaning algorithm was used for random data denoising, while a half-quadratic filter was applied to smooth and denoise the orientation maps. Grain area calculations were derived from grains which satisfied the $\omega \geq 15°$ condition, thus excluding the contribution of subgrains. A similar condition was set to study the evolution of grain form factor, calculated as a value from 1 to 4, where 1 represents equiaxed grains (width = length) and values above 1 represent elongated grains (width > length). Form factors of 1 were represented in blue, while elongated grains with from factors of 2 to 4 were represented with a green-orange-yellow color gradient. Kernel average misorientation (KAM) maps were calculated using a misorientation threshold from 0 - 3°, using a neighbor number of 2. Finally, the percentage of recrystallization was calculated using the grain orientation spread (GOS) method. In this case, grains which satisfied the $\omega \geq 15°$ were analyzed by calculating its average intra-granular misorientation by accounting for the presence of LAGBs and DDWs. If the average misorientation value was smaller than 1°, grains were assumed to be recrystallized and represented in blue color, i.e., misorientation from LAGBs and DDWs was negligible. Otherwise, grains were considered deformed and represented in red. This methodology has been used in the past to deconvolute deformed and recrystallized grains after FSP of Al and Cu alloys [24-26].

The large microstructural gradient (400 µm wide by 3.04 mm length) from base metal to processed zone was studied by using an area sectioning algorithm using the MTEX 5.8.2 toolbox. A total of 38 slices, with dimensions of 400 µm width and 80 µm height, were analyzed. For each slide, grain form factor, KAM and GOS maps were generated following the methodology previously described. Additionally, the percentage of LAGBs and recrystallized grains, as well as the average values of misorientation (2 - 61°), and KAM (0 - 3 °) of each slice were retrieved to reveal the position sensitive microstructural evolution in the direction towards the extrusion zone.

3.0 Results

- Site-specific measurements along different radial positions of the billet:

Figure 3 below a) to d) show the evolution of force and torque (a), extrusion feed rate and die rotation speed (b), thermoelectric voltages, and calibrated thermoelectric temperatures (d) during FE using a tool rotation speed of 150 RPM and a feed rate of 8 mm.min-1. During the early stage of FE (0 - 15s), the extrusion force and torque (Figure 3 a) show a sharp increase to maximum values of 163 kN and 635 N.m, respectively. Then, a fast process of relaxation occurs within 15 and 25 s, followed by a slower asymptotic behavior where the extrusion force and torque values approach steady state conditions around 76 kN and 368 N.m, respectively. The die rotation speed also tends to stabilize after approximately 15 s, while the extrusion feed rate remains stable througout the whole FE proecess (Figure 3 b)

Regarding TE measurements (Figure 3 c), there is a sharp increase in the electric potentials measured at Ni(1), Ni (2), Ni (3), and Ni (4) TE junctions during the initial 15 s of FE, followed by an asympthotic stabilizaiton during the steady state stage. The serrated behavior in the electric potential curves is caused by a sequence of Ni wire fractures as the billet is extruded. However, an uninterrupted electric potential measurement is possible since new TE junctions are forming in situ at the cross section of the freshly fractured wire tips. A similar serrated trend occurs in the TE temperature curves (Figure 3 d). Temperature drops are expected since the newly formed Al/Ni TE junctions occur at deeper positions relative to the die/billet interface. Despite the process of continous wire fractures, the heating cycle described by conventional thermocouples and TE junctions exhibit a similar behavior. Overall, the internal TE measurements are ~ 50 °C lower than the temperature at the die/billet interface. The final tempearture reads at the TE junction Ni (1), Ni (2), Ni (3), and Ni (4) are 531, 522, 526, and 511°C, respectively.

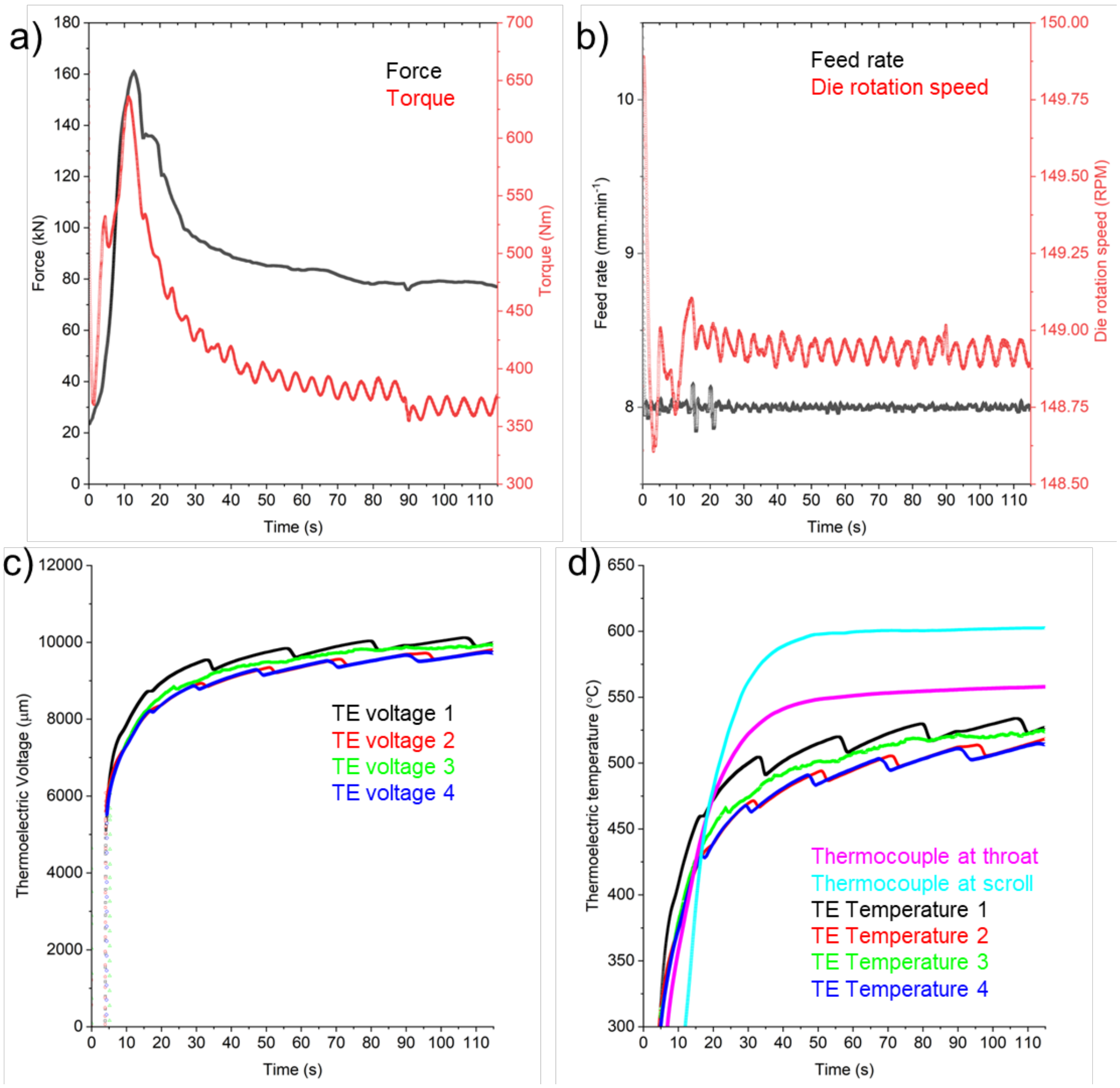

Figure 3. Friction extrusion of an instrumented Al1100 billet at 150 RPM rotation die speed and 8 mm.min-1 feed rate: a) force and torque; b) feed rate and die rotation speed; c) thermoelectric voltages measured at positions Ni (1) to Ni (4); d) calculated temperature profile from positions Ni (1) to Ni (4). Conventional contact thermocouple measurement at the H13 steel die within the throat and scroll regions are also shown in d) for comparison.

- Measurements at the extrusion center line for different extrusion feed rates:

Figure 4 below a), b), c) and d) show the temperature profiles measured using Al/Ni TE junctions (red) and conventional contact thermocouples at the die/billet interface (black) at different extrusion rates of 2, 8, 32, and 80 mm.min-1, respectively. The Al/Ni TE measurements correspond to the central position (0 radius).

Two behaviors can be noticed during the process of FE using the TE method. Firs, at slower extrusion feed rates (2 and 8 mm.min-1), stable thermal cycles with asymptotic values towards

550 and 526 °C develop over time. In both cases, the TE temperature curves are consistently below (~40 – 60 °C) conventional thermocouple measurements, consistent with the observations in Figure 3 d) at different radial positions. At faster extrusion feed rates (32 and 80 mm.min-1), there is a short initial stable heating stage, followed by an unstable stage described by large temperature drops due to premature Ni wire fractures. The maximum temperatures measured at the end of FE at 32 and 80 mm.min-1 were 478 and 344 °C, respectively.

Figure 4 e) and f), depict the evolution of the extrusion force and torque for all FE cases. Upon slow extrusion feed rates (≤ 8 mm.min-1), the extrusion force and torque profiles drastically decrease as the steady state stage develops. However, the faster extrusion feed rates (> 8 mm.min-1) lead to abrupt increments in extrusion force and torque during the initial FE stage and are not able to reach the second steady state stage. The relative peak extrusion and torsion stresses are shown in Figure 5. The larger extrusion and torsional stresses achieved within the billet during FE at fast feed rates of 32 and 80 m.min-1, in addition to the lower processing temperature led to harsh deformation conditions and premature failure of the TE junctions. A summary of the measured temperatures, forces, and stresses during FE is available in Table 2.

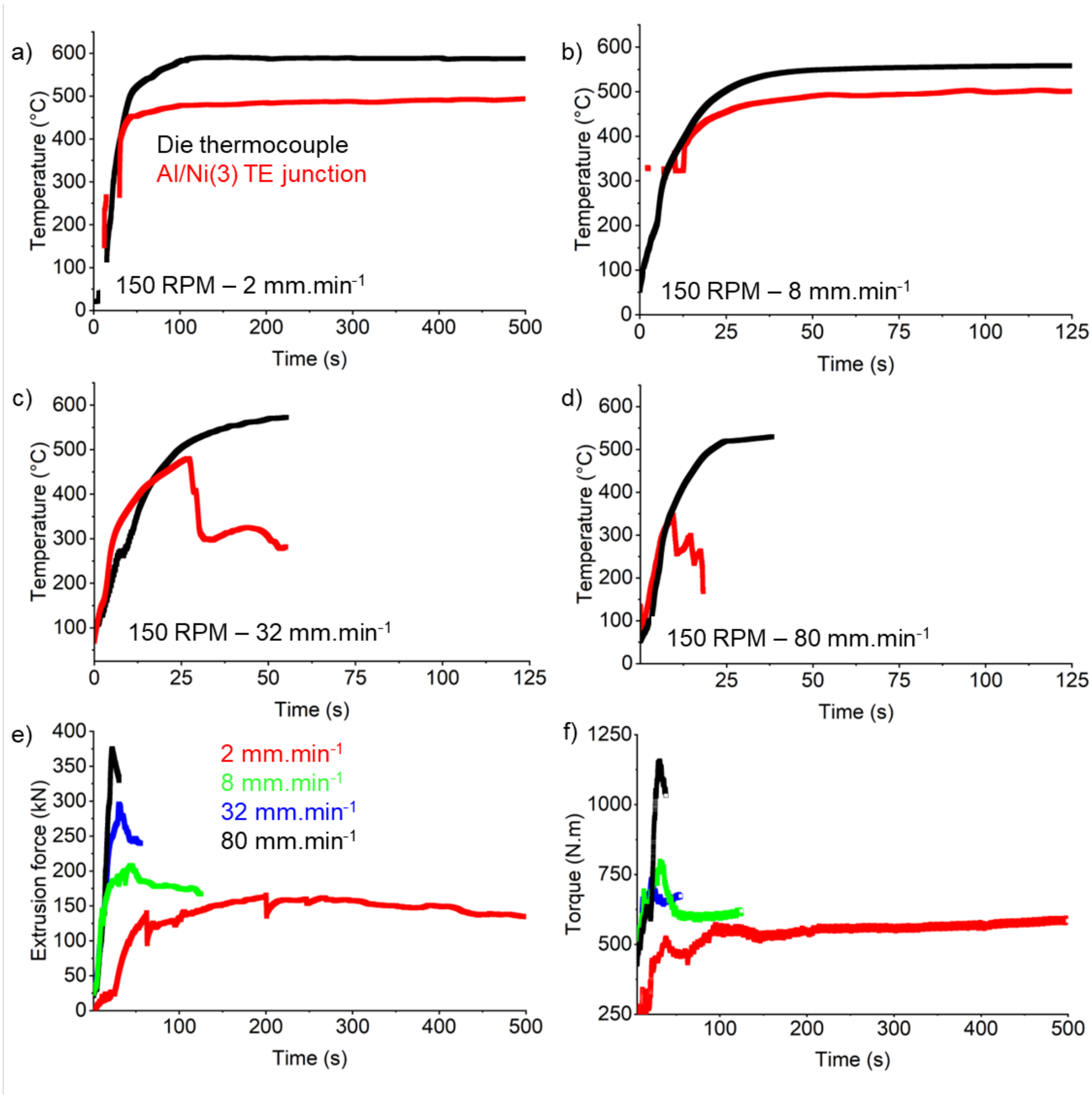

Figure 4. Friction extrusion of instrumented Al 1100 billets at 150 RPM die rotation speed and different feed rates: a), b), c) and d) show the comparison of the thermal profiles measured by the H13 die thermocouple at the throat region and the Ni (3) central thermoelectric junction measurements for extrusion feed rates of 2, 8, 32, and 80 mm.min-1; f) and g) show the evolution of the extrusion force and torque, respectively.

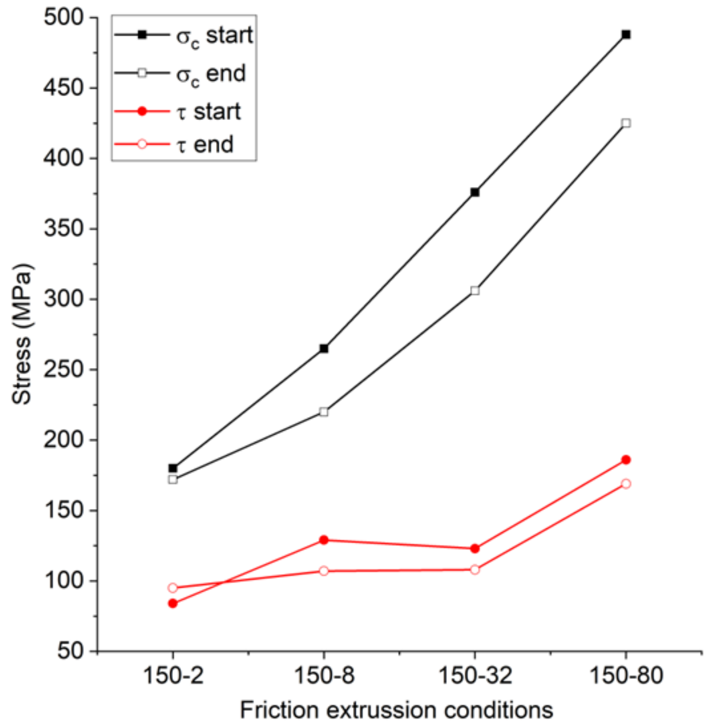

Figure 5. Average stresses during friction extrusion of instrumented Al1100 billets: Compressive and torsion stresses measured for a fixed 150 RPM die rotation speed and different feed rates of 2, 8, 32, and 80 mm.min-1. Solid and open symbols represent calculations retrieved from peak and final extrusion conditions, respectively.

Table 2. Summary of experimental measurements during friction extrusion of Al 1100 billets: A fixed die rotation speed of 150 RPM and different extrusion rates of 2, 8, 32 and 80 mm.min-1 were tested. The * symbols indicate premature fractures during thermoelectric measurements.

Die rotation speed (RPM) / extrusion feed rate (mm.min^{-1})	Force start (kN)	Force end (kN)	Torque start (Nm)	Torque end (Nm)	Die thermocouple at throat (°C)	Thermoelectric temperature (°C) at center position Ni (3)
150-2	170	100	460	492	609	530
150-8	163	76	635	368	560	526
150-32	295	240	761	670	553	478*
150-80	285	285	1065	910	544	344*

- Microstructural characterization at the vicinities of the thermoelectric junctions

After interrupted FE at 150 RPM and 8 mm.min-1, X-ray computed tomography scans were performed to retrieve the coordinates of the Al/Ni TE junction fractures. Figure 6 a) shows the top view of the billet and the deformed Ni (1), Ni (2), Ni (3), and Ni (4) wires. The rotational plastic flow at the processing zone (PZ) induces wire bending for the offset Ni(1), Ni(2), and Ni(4) wires. The offset Ni (2) and Ni (3) wires are arranged tangentially to the outer diameter of the die throat, while the center Ni(3) wire remains straight. Figure 6 b) shows the stacking of XCT scan results (filtered for Ni) and a LOM image of the transverse plane of the billet after etching. The fracture positions of the AL/Ni TE junctions are indicated by red circles. Red arrows indicate the apparent directionality of the plastic flow, separating the PZ from the thermomechanically affected zone (TMAZ), evidencing a W-shaped deformation zone profile. The Ni(1), Ni(2), and Ni(4) junctions break within the TMAZ while the central Ni(3) reaches approximately half way into the PZ.

Figure 6 c) depicts a LOM image at the transverse section (a - a), which is a co-planar cut to the Ni (3) and Ni (4) fractures. Microstructural analysis at the vicinities of the Ni(3) and Ni(4) TE junction fractures are shown via EBSD in Figure 6 d) and e), respectively. HAGBs are highlighted by bold black lines, while LAGBs are shown in light gray. Refined and recrystallized Al grains appear near the Ni(3) fracture zone within the PZ, where the TE temperature measurement corresponds to ~522 °C. However, near the Ni(2) TE junction fracture, coarser and more elongated Al grains can be seen in Figure 6 e). The measured TE temperature near this transitioning region near Ni(4) is ~511 °C.

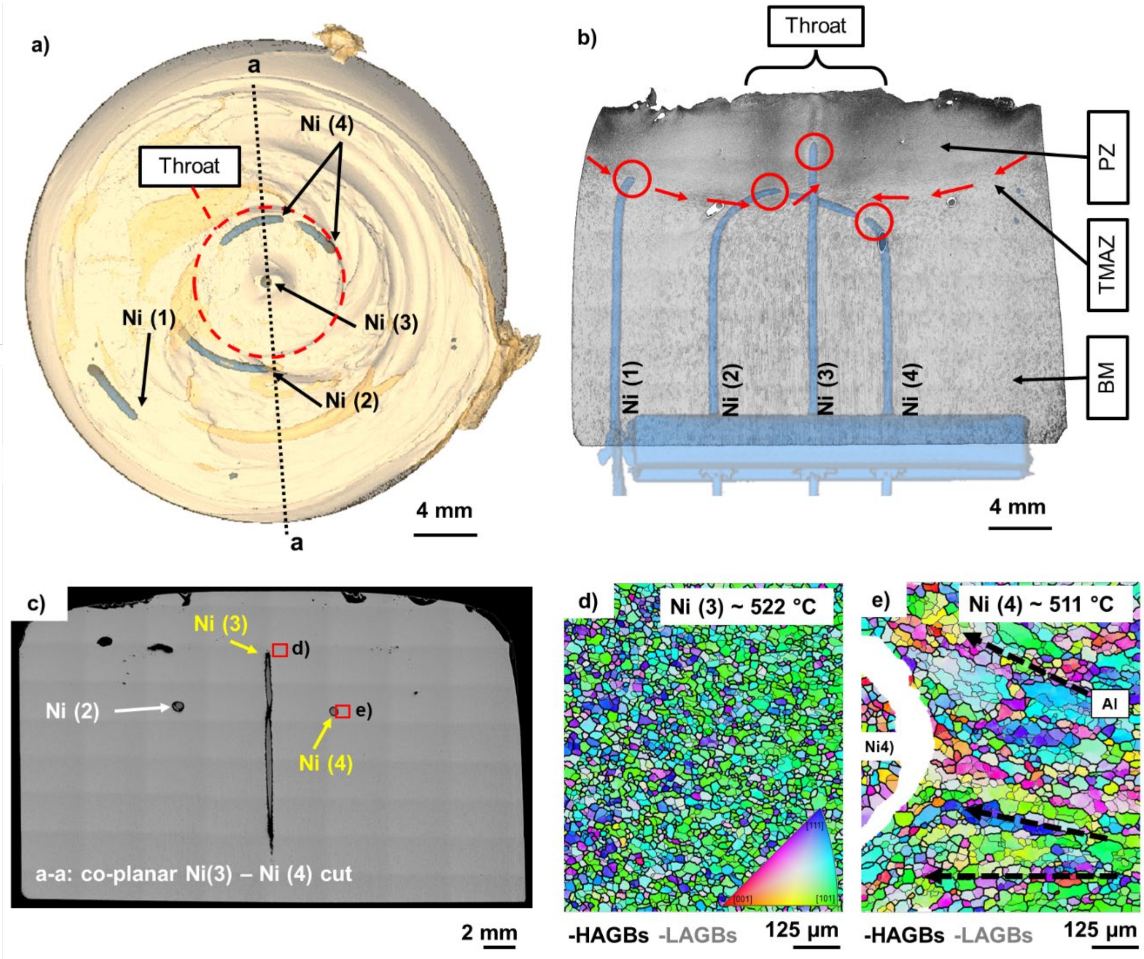

Figure 6. Microstructural analysis after friction extrusion of an instrumented Al 1100 billet at a die rotation speed of 150 RPM and a feed rate of 8 mm.min-1: a) Top view of the XCT scan analysis showing the position of the Ni (1), Ni (2), Ni (3), and Ni (4) wires inside the Al billet; b) XCT scan filtered for Ni overlaid on a LOM image of the billet transverse section after etching; c) LOM image of the a-a plane containing the fractures of the thermoelectric junctions Ni (3) and Ni (4); d) and e) show inverse pole figures in the Z direction retrieved at the vicinities of the Ni(3) and Ni(4) fractures, respectively. Red circles in b) indicate the position of the Al/Ni TE junction fractures. Red arrows in b) show the directionality of the plastic flow described by the etched microstructure.

- Smooth particle hydrodynamic modeling of FE at 150 RPM and 8 mm.min-1

Figure 7 summarizes SPH modeling results obtained for steady state FE at 150 RPM and 8 mm.min-1. Results are separated into two sections: center plane of extrusion at 0 radius (a, c, e, and g), and an offset plane representing the position of a side Al/Ni TE junction fracture (b, d, f, and h) based on XCT. In all cases, XCT scan images of the Ni wires are overlaid to the SPH simulation results to provide a more comprehensive description of the microstructural evolution during FE. Temperature (Figure 7 c, d), strain (Figure 7 e, f), and strain rate (Figure 7 g, h) simulations are presented. Additionally, line profiles retrieved at 0 radius and at 6.4 mm radius, i.e., position of Ni(2) are provided for the center plane temperature, stress and strain fields. The Y coordinates of the Ni(3) and Ni(2) fractures are highlighted by gray and red stars for comparison. Results are discussed as follows:

- Simulated thermal field:

The simulated thermal fields at the center and offset planes of extrusion are depicted in Figure 7 c) and d). The black solid circles and the dashed black circle in Figure 7 c) depict final positions of TE temperature measurements, as well as the position of the conventional thermocouple at the die/billet interface, respectively. Similar temperature distributions can be seen at the center and offset planes. Overall, there is a reasonable agreement between measured and simulated temperatures, with average deviations within ± 5 °C for the TE junctions Ni (2), Ni (3), Ni (4) and the conventional thermocouple, and 17 °C for Ni (1). Experimental and simulation results show that the hottest spots within the billet are located near the outside diameter underneath the scroll at the billet/die interface. A decreasing thermal gradient develops in the direction towards the base of the billet. However, the temperature field at the center plane seem to also follow a W-shaped distribution since the temperature line profiles at the Ni(2) radial distance reaches higher temperature values sooner relative to the 0 radius Ni(3) position.

- Simulated strain field:

Figure 7 e) and f) show the calculated W-shaped strain fields at the center and offset planes, respectively. A rapid train increase from the BM towards the PZ can be seen in both cases by the formation of a relatively short low strain zone (green), followed by a dominant large strain zone (brown). The line profile strain analysis at the Ni(2) and Ni(1) wire positions shows an exponential increase in both positions. However, larger strains are obtained earlier at the Ni(2) position relative to the 0 radius region. Notice the strain map is plotted between 0 and 0.1 to better represent the small strain transitioning zones near the BM. A strain map with a linear scale plot is available in the supplementary section (Figure S1).

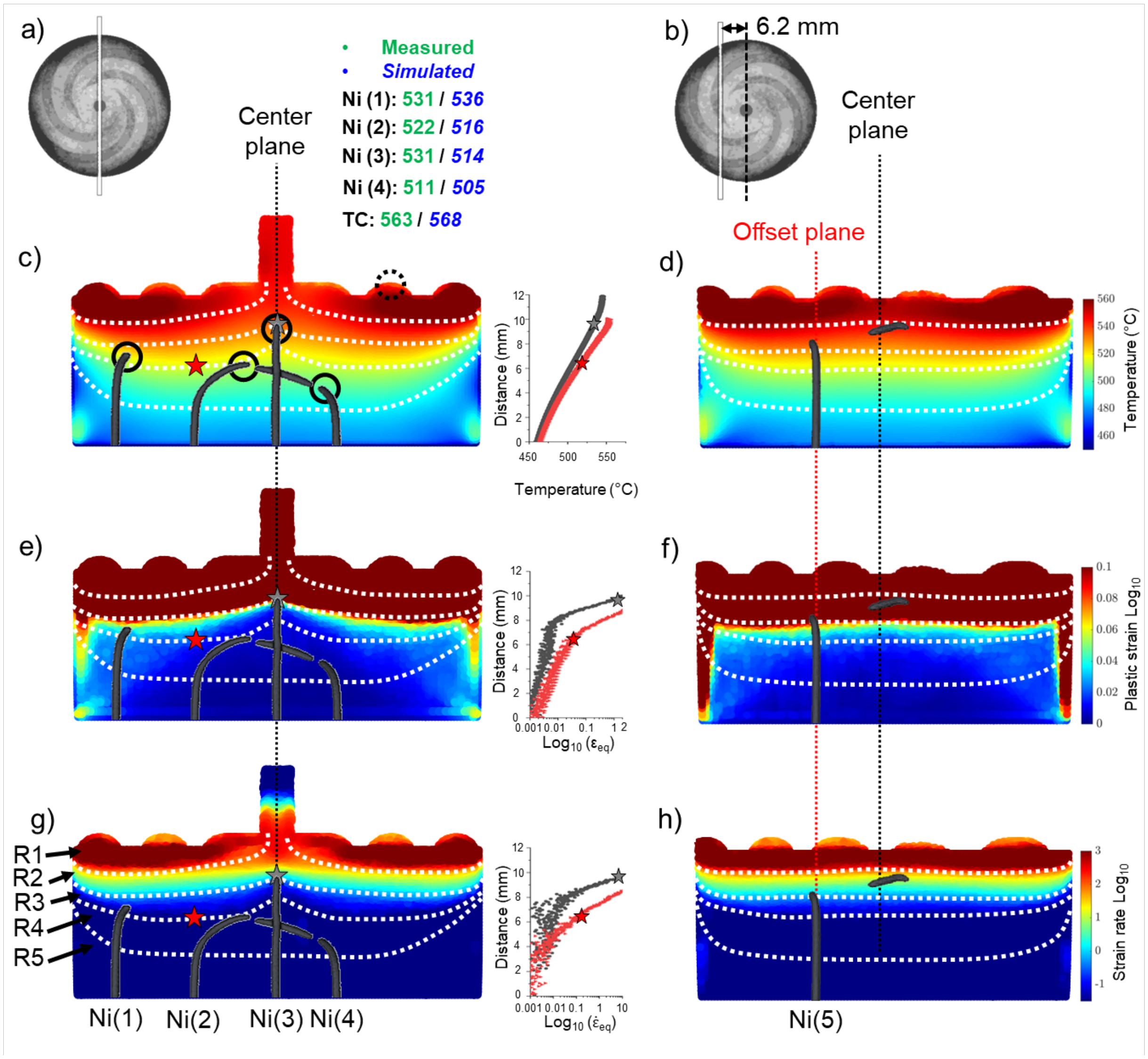

Figure 7. SPH modeling of FE of an Al1100 billet for a die rotation speed of 150 RPM and a feed rate of 8 mm.min-1: a) and b) show the transverse sections of the billet retrieved at the center plane of extrusion and at an offset plane of a Ni wire fracture based on XCT scan coordinates, respectively. The relative thermal fields are shown in c) and d); while the strain and strain rate fields are depicted in e), f), and g), h), respectively. XCT scan results filtered for Ni are overlaid to the SPH results to aid visual comparisons. Line profile temperature, strain, and strain rate profiles profiles retrieved along the zero radius and the Ni (2) radial position at the center plane transverse section are also shown. The red and gray starts in c), e), and g) represent the Y coordinate positions of the Ni (2) and Ni (3) wires, respectively. Different microstructural regions, namely R1 to R5, are highlighted by white arrows in all cases. The solid and dashed circles in c) represent internal thermoelectric temperature positions and conventional contact thermocouple measurements, respectively.

- Simulated strain rate field:

Figure 7 g) and h) depict the calculated W-shaped strain rate fields at the center and offset planes respectively. Similar to the strain field case, very sharp transitions between low and high strain rate fields appear in both planes. Line profile analysis also show the exponential grow of the strain rate at the Ni(2) and 0 radius positions at the center plane. Regions of the microstructure located near Ni(2) experience earlier and larger strain rates relative to the center line. A very large strain rate zone becomes apparent underneath the scroll region at the die/billet interface. This region undergoes the largest overall strain rate due to forced plastic flow through the scrolls towards the die throat.

Based on the SPH modeling results, five distinctive microstructural regions, namely R1-R5 can be observed (Figure 7 g). First, R1 is a high temperature, and very high strain and strain rate region which can be interpreted as the heavy processed zone (hPZ) underneath the die scrolls, feeding into the die throat zone. Region R2 is a milder processing zone (mPZ) underneath the direct effect of the scroll die plastic zone, consisting of a gradient of lower extrusion temperatures, strain, and strain rates. The third zone R3 is the TMAZ consisting of comparatively mild strain and strain rate gradients and lower temperature. Region R4 can be understood as a relatively long TMAZ/HAZ transitioning zone. Finally, region R5 represents the HAZ where strain and strain rate contributions are negligible.

- Microstructural validation of FE at the maximum strain and strain rate zone

Experimental and SPH simulation results indicate that a Ni wire positioned along the mid-radius length, for example near the Ni(2) position, undergoes the earliest fracture during FE. Therefore, a second partially extruded sample with a side Ni wire labeled as Ni(5) was cut along the offset plane described in Figure 7 b). More details into the XCT scan and metallographic polishing used to precisely expose the microstructure along the Ni(5) fracture are available in the supplementary section (Figure S2).

Figure 8 a) shows a LOM image overlaid with a large EBSD montage, depicting the microstructural transition from the BM/HAZ towards the mPZ for the Ni(5) wire case. Figure 8 b) presents line profile analyses of temperature and strain retrieved at the Ni(5) radial position as described in Figure 7 b). Additionally, maps showing the evolution of grain morphology (i.e., form factor), kernel average misorientation, and activation of recrystallization are depicted in Figure 7 c), d) and e), respectively. Local average values of percentage of LAGBs, average misorientation, average KAM between 1-3°, and percentage of recrystallized grains for 38 data subsets are also shown. Additionally, the quantification of grain area and grain form factor evolution along the BM/HAZ/TMAZ/mPZ microstructural transition is summarized in Figure 9. The microstructural evolution is divided into mPZ, TMAZ, and HAZ, and is discussed as follows.

- Base metal / heat affected zone:

The microstructure at the BM/HAZ transition shows elongated grains with an average form factor of ~3.5 and large sizes of~ 700 µm2. The lowest average misorientation (~ 15°), percentage of recrystallization (0 – 2 %), and the highest percentage of LAGBs (~ 25%) are observed within this region.

- Heat affected zone / thermomechanically affected zone:

The HAZ/TMAZ transition is described by the mild reduction in average KAM (0.78 to 0.65) in the direction towards the processed zone. This is caused by the effect of temperature relaxation up to 495 °C under negligible straining conditions.

- Thermomechanically affected zone / mild processed zone:

The increasing temperature profile of 495-500 °C and small strain of 2-3% induce slight grain reorientation following the plastic flow. Less equiaxed grains with average factor factors of ~ 1.8 appear as the microstructure approaches the mPZ. The local thermomechanical cycle induces a decrease in LAGBs (30 to 5%), further intra-granular relaxation (KAM values around 0.65 to 0.55°), and activation of recrystallization (0 – 12%), leading to an overall increase in the average high angle microstructural misorientation (15 to 30°).

- Mild processed zone:

The microstructure within the mild processing zone shows increasing gradients of temperature (500 – 510 °C) and strain (3-8%) in the direction towards the heavy processed zone. The local microstructure consists of the coexistence of approximately equiaxed grains (average form factor < 1.5) and elongated grains (average form factors between 3 and 4). Overall, the most refined grain sizes (~ 25 μm2), lowest percentage of LAGBs (~ 5%), lowest KAM values (~ 0.52°), the highest percentage of recrystallized grains (~ 12-15%), and the highest overall high angle misorientation (~ 30°). Detailed images of these local microstructures are provided in the supplementary section (Figure S3)

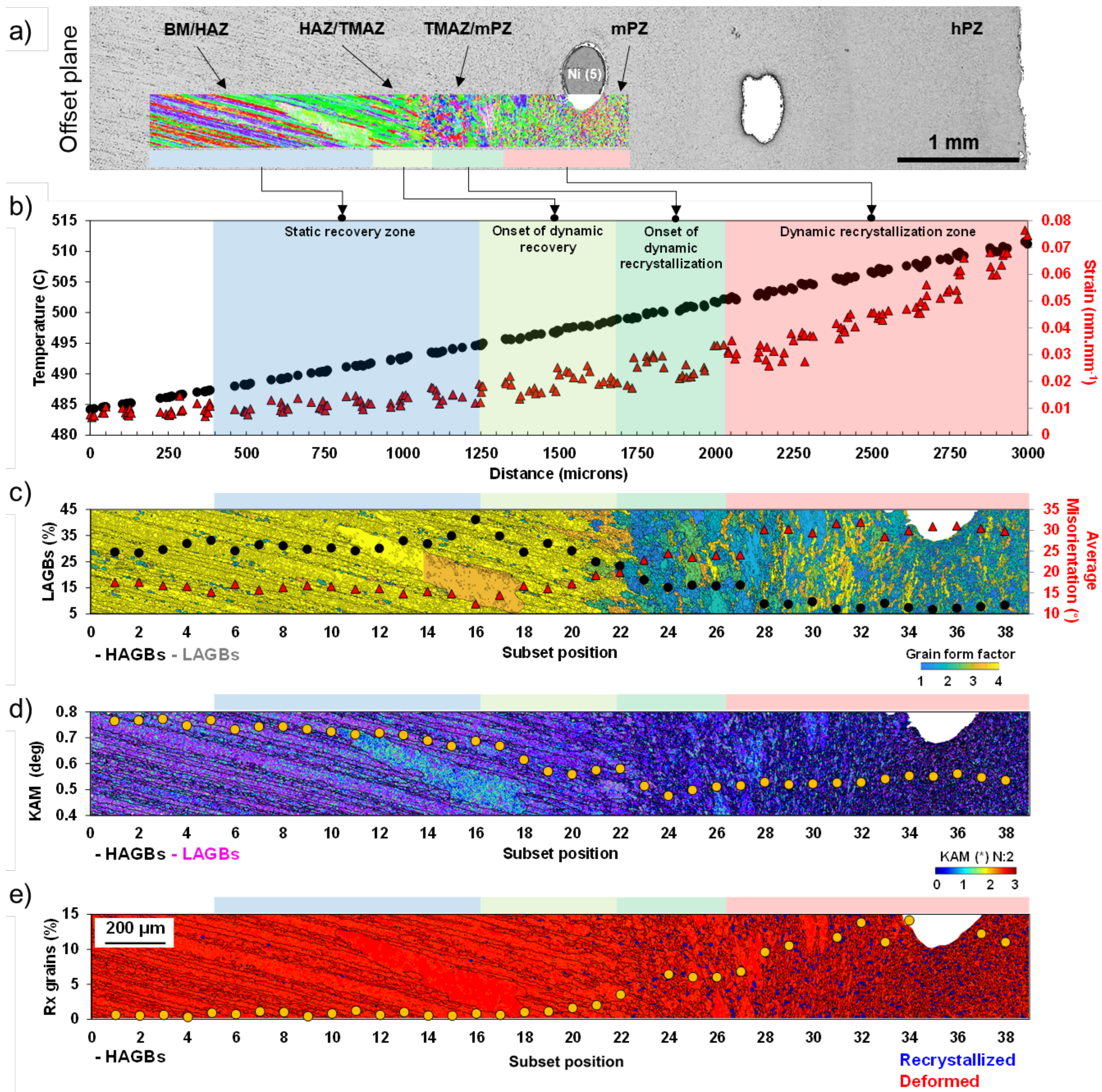

Figure 8. Microstructural validation along the offset plane of the Ni (5) wire thermoelectric junction after interrupted FE of an instrumented Al 1100 billet for a die rotation speed of 150 RPM and a feed rate of 8 mm.min-1: a) LOM image overlaid with a large EBSD montage showing the transition from BM to mild processed zone at the vicinity of the Ni (5) wire fracture; b) SPH-based temperature and strain line profile calculation along the BM/HAZ/TMAZ/mPZ transition; c) evolution of grain form factor (blue: equiaxed; yellow: elongated) overlaid with the quantification of average misorientation and percentage of low angle grain boundaries; d) kernel average misorientation map overlaid with the average local values; e) grain orientation spread map defining the ratio of deformed (red) to recrystallized (blue) grains overlaid with the local percentage of recrystallized grains. In c) to e), each point represents the average values retrieved from subset areas of 340 µm length and 80 µm height, for a total of 38 subsets.

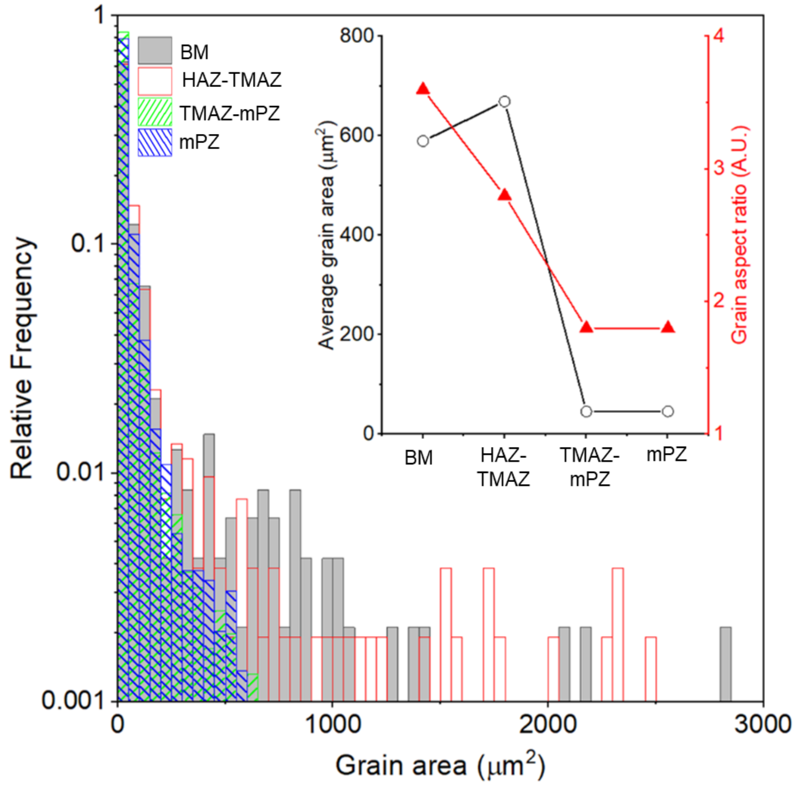

Figure 9. Evolution of grain area and grain form factor: base metal, HAZ-TMAZ transition, TMAZ-mPZ transition, and mPZ.

4.0 Discussion

Site-specific internal temperature measurements inside the extruding billet are possible by the accurate measurement of thermoelectric voltage under careful electric insulation. Our results clarify that measurements can be obtained uninterruptedly by in situ generation of TE junctions, but that there is a limit to the probing depth along the radial direction. Three important aspects regarding TE are described as follows.

- Asymmetric probing depth

Figure 10 a) and b) show a schematic representations of the plastic flow inducing Ni wire bending and fracture during FE seen from top and side views respectively. The development of deeper probing depths at zero radius and near the outer diameter, and minimum probing depths at around Ni (4) can be explained by local differences in radial velocity and stress conditions. Figure 10 c) shows the schematic representation of Ni wire bending away from the centerline. The Ni wire tips experience a combination of compressive forces (Fz), torque from a radial force tangential to the plastic flow (Fr), and a tractive force at the wire tip as it gets pulled towards the die throat zone (Ft). The gradient of radial velocities along the radial direction leads to different degrees of wire bending for Ni (1), Ni (2), and Ni (4), and thus different equilibrium measurement positions. On the other hand, Figure 10 d) depicts how the Ni wire tip at 0 radius undergoes mostly compressive strain with a very small torque and no tractive force. The combination of temperature and the spiral-like plastic flow at the tip of the center Ni wire is expected to cause a compressive-torsion like fracture. Finally, Figure 10 e) and f) show the process of in situ formation of new TE junctions at the fresh fracture zone, while the fractured pieces are extruded following the Al plastic flow.

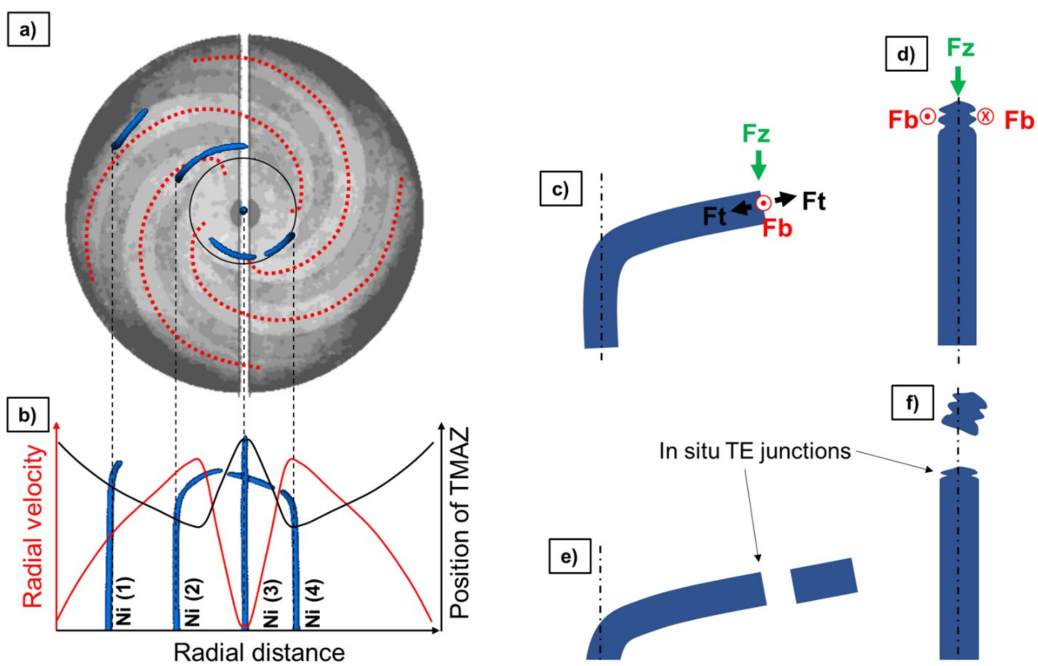

Figure 10. Schematic representation of the process of thermoelectric voltage measurements during FS: a) top view of the extrusion die overlaid with XCT scan results filtered for Ni; b) radial velocity and position of the TMAZ along the radial direction overlaid with XCT scan results filtered for Ni; c) and d) show the process of wire bending and local

forces at the wire tips for offset and zero radius cases, respectively; e) and f) depict the process of wire tip fracture, disconnection, and in situ generation of fresh thermoelectric junctions.

Previous SPH-based modeling of friction back extrusion of Al tube shapes [27] showed that the velocity of the plastic zone at the billet is minimized at 0 radius and increases in the direction towards the outer diameter. Furthermore, SPH simulations using marker materials placed at zero radius and at 1/3 radius in an Al billet show the development of a spiral-like plastic flow towards the extrusion hole and preferential bending of the marker material at 1/3 radius [28]. Experimental results from Halak, et al. [29] and Suhuddin et al. [30], also evidenced the formation of a low shear zone near 0 radius, and the appearance of a w-shaped deformation profile at the cross section of the processing zone during friction extrusion of Al. However, the width of the low strain zone near zero radius can be modified by modifying the die throat geometry or by increasing the extrusion force [29]. The latter is consistent with our experimental observations as a function of the extrusion feed rate (Figure 4), where faster extrusion feed rates lead to earlier fractures of the Al/Ni TE junctions, including the ones located at zero radius.

- Serrated voltage signal

Smaller fractures and the development of a steadier internal temperature measurement occur over time at the Al/Ni TE junction at zero radius relative to off center junctions (Figure 3). During FE, the fractured wire fragments are instantaneously disconnected from the TE circuit and the voltage read resumes immediate at the new point of contact at a smaller depth (Figure 10 e, f). This results in a serrated voltage curve format over time. The enamel coating applied to the perimeter of the Ni wires is key to maintain electrical isolation everywhere except for the exposed cross section of the freshly fractured tip. The insulating barrier remains cohesive during FE, while an additional oxide layer develops at the Al billet and enamel coating interface. Further details showing EDS analysis at the Ni wire – enamel coating – Al billet interface are available in the supplementary section (Figure S4).

Thermoelectric temperature measurements during FSP [10, 16] and friction welding [19] normally exhibit relatively stable readings over time. This can be expected since in the former cases the TE junctions were generated by two rigid bodies, i.e., the FSP tool and the workpiece [10, 16] or by two rotating cylinders rammed onto each other [19]. Our current investigation zone. This serrated behavior is maximized near the outer diameter of the billet and minimized at zero radius due to the influence of maximum and minimum bending forces, respectively. More details into the serration behavior at different radial positions for feed rates of 2, 8 and 80 mm.min-1 are provided in the supplementary section (Figure S5).

- Asymmetric temperature profile

Our results provide evidence of the development of an asymmetric thermal field along the transverse section of the billet during FE. Thermoelectric temperature measurements in Figure 3 d) and supplementary figure SX show how the Al/Ni TE junctions near the outer diameter exhibit the highest overall temperature reads at slow and very fast feed rates. This behavior is also observed via conventional thermocouple measurements (Figure 3 d) when comparing the throat area (colder) and the region underneath the scrolls at x/x radial position (hotter).

During solid state processing, such as for FSP and FE, heat generation occurs due to frictional sliding between the tool/die and the workpiece/billet, and by the strong plastic deformation experienced by the material underneath the tool/die [27, 31]. According to Li, el al., during the shear assisted processing and extrusion of Al tubes, 80% of the steady-state heat generation during FE can be attributed to plastic dissipation, while the remaining 20% is associated to mandrel/billet and die/billet frictional sliding [27]. Our SPH modeling results show that, in addition to the w-shaped temperature distribution, there are two hot spots located right underneath the scroll/billet interface near the outer diameter (Figure 7 a). These hotspots are therefore associated to the strong plastic deformation and heat dissipation right underneath the direct action of the scrolls. This asymmetric temperature profile leads to the formation of a core-shell microstructure at the extrudate, as shown in the Supplementary Section (Figure SX).

- Graded dynamic recovery and recrystallization during FE

The microstructural transition from BM to PZ is not homogeneous and strongly depends on the distance to the 0 radius axis of symmetry. Earlier and harsher processing conditions occur for the microstructural regions around 4.6 to 6.6 mm from the centerline, i.e., at the Ni (2) and Ni (4) TE junction positions. Whereas delayed microstructural evolution occurs along the centerline. Strain and strain rate are the most important factors driving fast microstructural refinement and alignment along the plastic flow direction. For example, the temperature difference at the fracture regions near Ni (3) and Ni (2) is only 10 °C. However, such microstructures strongly differ, with the Ni (3) zone consisting of dynamically recrystallized grains, and the Ni (2) zone rather exhibiting dynamically recovered coarse and elongated grains (Figure 6 d, e).

The microstructural transition from BM to PZ during FE is remarkably similar to that obtained after FSW of Al alloys. For example, Mironov et al., reported a comprehensive microstructural analysis along the BM/TMAZ/SZ transition after FSW of an Al1050 [32]. Results show that the initially elongated BM Al grains first undergo tilting along the plastic flow direction within the TMAZ with limited grain refinement. Then, grain form factor and size reduction occurs across the TMAZ/SZ interface leading to dynamically recrystallized grains within the SZ [32]. As a general trend, aluminum alloys have a large stacking fault energy and preferentially undergo recovery as the main static restoration mechanism, and continuous dynamic recrystallization when strain and temperature are applied simultaneously [33]. However, the microstructural evolution of previously deformed initial microstructures during solid phase processing can be complex and should be separated into smaller zones. First, at overlapping regions, such as the HAZ/TMAZ case, the kinetics of dislocation recombination and microstructural softening is governed by static recovery (at the HAZ), and is accelerated via dynamic recovery (at the TMAZ) even under mild strain rates [33-35]. During this process, dense dislocation walls and low angle grain boundaries slowly evolve into high angle grain boundaries as more deformation is applied [26, 34, 36]. However, at regions with larger strain, strain rates, and deformation temperatures, such as the TMAZ/SZ, the kinetics of dynamic recovery is further accelerated by the activation of continuous and geometric dynamic recrystallization [26, 37-39].

So far, our experimental observations during FE are consistent with the mechanisms reported in literature for FSP. First, the HAZ/TMAZ transition is governed by a gradient of static and dynamic recovery. The TMAZ/mPZ transition shows progressive grain refinement and bending, thus activating continuous and geometric dynamic recrystallization mechanisms. The mPZ and hPZ are rather advanced stages of grain refinement and can be understood generically as dynamically recrystallized.

5.0 Conclusion

This work demonstrates for the first time the concept of thermoelectric site-specific measurements inside the deformation zone during friction extrusion experiments. This was possible by the instrumentation of Al1100 cylindric billets with enamel coated Ni wires located along different radial positions of the billet at known probing depth. Targeted microstructural characterization at the precise points of thermoelectric contact was possible by the combination of X-ray computed tomography and electron backscatter diffraction. Additionally, smooth particle hydrodynamic modeling was used to further understand the thermal, strain, and strain rate fields developing during steady state FE.

Our results show that electric potentials can be measured simultaneously at several Al/Ni thermoelectric junctions inside the deformation zone during FE at different extrusion feed rates. The maximum probing depths are achieved at zero radius and near the outer diameter of the billet due to the development of w-shaped asymmetric temperature, strain, and strain rate fields. A continuous process of Ni wire tip fracture occurs during FE, but uninterrupted thermoelectric measurements are possible via the in situ generation of fresh thermoelectric junctions. Measurements immediately resume at the newly formed Ni wire cross sections - Al matrix points of contact.

The current internal temperature measurement results, paired to conventional contact thermocouples and smooth particle hydrodynamic simulations allowed to confirm the asymmetric temperature distribution arising during steady state FE. The hottest regions of the billet are located immediately underneath the die scrolls at the die/billet interface and are caused by the very large strain and strain rates experienced by the plasticized Al. The linear decrease in temperature and the exponential decrease in strain and strain rate in the direction towards the base metal generate a rich variety of microstructural transitions that are remarkably similar to friction stir processing. Static recovery occurs within the heat affected zone, while a gradient of dynamic recovery, continuous and geometric dynamic recrystallization are activated between the thermomechanically affected zone and the mild processing zone.

6.0 References

[1] N.R. Overman, S.A. Whalen, M.E. Bowden, M.J. Olszta, K. Kruska, T. Clark, E.L. Stevens, J.T. Darsell, V.V. Joshi, X. Jiang, K.F. Mattlin, S.N. Mathaudhu, Homogenization and texture development in rapidly solidified AZ91E consolidated by Shear Assisted Processing and Extrusion (ShAPE), Mat Sci Eng a-Struct 701 (2017) 56-68.

[2] S.O. Whalen, Matthew; Roach, Christian; Darsell, Jens; Graff, Daniel; Reza-E-Rabby, Md.; Roosendaal, Timothy; Daye, Wayne; Pelletiers, Tom; Mathaudhu, Suveen; Overman, Nicole., High ductility aluminum alloy made from powder by friction extrusion, Materialia 6 (2019) 100260.

[3] X. Li, C. Zhou, N. Overman, X.L. Ma, N. Canfield, K. Kappagantula, J. Schroth, G. Grant, Copper carbon composite wire with a uniform carbon dispersion made by friction extrusion, J Manuf Process 65 (2021) 397-406.

[4] X.L. Ma, E. Nickerson, T.H. Wang, D.L. Zhang, T. Pelletiers, S. Whalen, X. Li, Friction extrusion of ODS copper rod made from powder, J Manuf Process 84 (2022) 223-229.

[5] F. Abu-Farha, A preliminary study on the feasibility of friction stir back extrusion, Scripta Mater 66(9) (2012) 615-618.

[6] T.H. Wang, J.E. Atehortua, M. Song, M. Reza-E-Rabby, B.S. Taysom, J. Silverstein, T. Roosendaal, D. Herling, S. Whalen, Extrusion of Unhomogenized Castings of 7075 Aluminum via ShAPE, Mater Design 213 (2022).

[7] S. Whalen, M. Olszta, M. Reza-E-Rabby, T. Roosendaal, T.H. Wang, D. Herling, B.S. Taysom, S. Suffield, N. Overman, High speed manufacturing of aluminum alloy 7075 tubing by Shear Assisted Processing and Extrusion (ShAPE), J Manuf Process 71 (2021) 699-710.

[8] M. Komarasamy, X. Li, S.A. Whalen, X.L. Ma, N. Canfield, M.J. Olszta, T. Varga, A.L. Schemer-Kohrn, A.Q. Yu, N.R. Overman, S.N. Mathaudhu, G.J. Grant, Microstructural evolution in Cu-Nb processed via friction consolidation, J Mater Sci 56(22) (2021) 12864-12880.

[9] N.R. Overman, M.J. Olszta, M. Bowden, X. Li, A. Rohatgi, S.N. Mathaudhu, G.J. Grant, S.A. Whalen, The onset of alloying in Cu-Ni powders under high-shear consolidation, Mater Design 211 (2021).

[10] J. De Backer, G. Bolmsjo, A.K. Christiansson, Temperature control of robotic friction stir welding using the thermoelectric effect, Int J Adv Manuf Tech 70(1-4) (2014) 375-383.

[11] S. Verma, Meenu, J.P. Misra, Study on temperature distribution during Friction Stir Welding of 6082 aluminum alloy, Mater Today-Proc 4(2) (2017) 1350-1356.

[12] K.A. Ross, Investigation and Implementation of a Robust Temperature Control Algorithm for Friction Stir Welding, Brigham Young University 2012.

[13] K. Ross, Sorensen, C., Advances in Temperature Control for FSP, Friction Stir Welding and Processing VII, Springer, Cham.2013.

[14] Y.H. Yau, A. Hussain, R.K. Lalwani, H.K. Chan, N. Hakimi, Temperature distribution study during the friction stir welding process of Al2024-T3 aluminum alloy, Int J Min Met Mater 20(8) (2013) 779-787.

[15] A.M. Wright, T.R.; Hovanski, Y., Evaluating Temperature Control in Friction Stir Welding for Industrial Applications, Journal of Manufacturing and Materials Processing 5 (2021).

[16] A. Silva-Magalhaes, J. De Backer, J. Martin, G. Bolmsjo, In-situ temperature measurement in friction stir welding of thick section aluminium alloys, J Manuf Process 39 (2019) 12-17.

[17] J.C. Heigel, E. Whitenton, B. Lane, M.A. Donmez, V. Madhavan, W. Moscoso-Kingsley, Infrared measurement of the temperature at the tool-chip interface while machining Ti-6Al-4V, J Mater Process Tech 243 (2017) 123-130.

[18] T.J. Seebeck, Ueber die magnetische Polarisation der Metalle und Erze durch Temperatur-Differenz, Annalen der Physik 82(2) (1826) 133-160.

[19] B.S. Taysom, X.L. Ma, S. Whalen, In situ temperature measurement of a deforming interface with thermoelectricity, T I Meas Control (2023).

[20] D.M. Rowe, CRC Handbook of Thermoelectrics, (2018).

[21] F. Bachmann, R. Hielscher, H. Schaeben, Grain detection from 2d and 3d EBSD data-Specification of the MTEX algorithm, Ultramicroscopy 111(12) (2011) 1720-1733.

[22] H. Jazaeri, F.J. Humphreys, Quantifying recrystallization by electron backscatter diffraction, J Microsc-Oxford 213 (2004) 241-246.

[23] P.J. Hurley, F.J. Humphreys, The application of EBSD to the study of substructural development in a cold rolled single-phase aluminium alloy, Acta Mater 51(4) (2003) 1087-1102.

[24] J. Escobar, B. Gwalani, J. Silverstein, T. Ajantiwalay, C. Roach, L. Bergmann, J.F. dos Santos, E. Maawad, B. Klusemann, A. Devaraj, Rapid grain refinement and compositional homogenization in a cast binary Cu50Ni alloy achieved by friction stir processing, Mater Charact 202 (2023).

[25] J. Escobar, B. Gwalani, M. Olszta, J. Silverstein, T. Ajantiwalay, N. Overman, W.K. Fu, Y.L. Li, L. Bergmann, E. Maawad, B. Klusemann, J.F.D. Santos, A. Devaraj, Heterogenous activation of dynamic recrystallization and twinning during friction stir processing of a Cu-4Nb alloy, J Alloy Compd 928 (2022).

[26] J. Escobar, B. Gwalani, M. Olszta, J. Silverstein, N. Overman, L. Bergmann, J.F. dos Santos, P. Staron, E. Maawad, B. Klusemann, S. Mathaudhu, A. Devaraj, Multimodal analysis of spatially heterogeneous microstructural refinement and softening mechanisms in three-pass friction stir processed Al-4Si alloy, J Alloy Compd 887 (2021).

[27] L. Li, M. Reza-E-Rabby, N. Overman, T.H. Wang, S. Whalen, G. Grant, S. Mathaudhu, A. Soulami, Analysis of contact conditions and microstructure evolution in shear assisted processing and extrusion using smoothed particle hydrodynamics method, Mater Design 221 (2022).

[28] L. Li, V. Gupta, X. Li, A.P. Reynolds, G. Grant, A. Soulami, Meshfree simulation and experimental validation of extreme thermomechanical conditions in friction stir extrusion, Comput Part Mech 9(4) (2022) 789-809.

[29] R.M. Halak, L. Rath, U.F.H.R. Suhuddin, J.F. dos Santos, B. Klusemann, Changes in processing characteristics and microstructural evolution during friction extrusion of aluminum, Int J Mater Form 15(3) (2022).

[30] U.F.H. Suhuddin, L. Rath, R.M. Halak, B. Klusemann, Microstructure evolution and texture development during production of homogeneous fine-grained aluminum wire by friction extrusion, Mater Charact 205 (2023) 113252.

[31] W.X. Pan, D.S. Li, A.M. Tartakovsky, S. Ahzi, M. Khraisheh, M. Khaleel, A new smoothed particle hydrodynamics non-Newtonian model for friction stir welding: Process modeling and simulation of microstructure evolution in a magnesium alloy, Int J Plasticity 48 (2013) 189-204.

[32] S. Mironov, K. Inagaki, Y.S. Sato, H. Kokawa, Effect of Welding Temperature on Microstructure of Friction-stir Welded Aluminum Alloy 1050, Metall Mater Trans A 46a(2) (2015) 783-790.

[33] F.J. Humphreys, M. Hatherly, Recrystallization and Related Annealing Phenomena, 2004.

[34] Y. Huang, F.J. Humphreys, I. Brough, The application of a hot deformation SEM stage, backscattered electron imaging and EBSD to the study of thermomechanical processing, Journal of Microscopy-Oxford 208 (2002) 18-23.

[35] A. Gholinia, F. Humphreys, P.B. Prangnell, Production of ultra-fine grain microstructures in Al-Mg alloys by coventional rolling, Acta Mater 50(18) (2002) 4461-4476.

[36] Y. Huang, F.J. Humphreys, Transient dynamic recrystallization in an aluminium alloy subjected to large reductions in strain rate, Acta Mater 45(11) (1997) 4491-4503.

[37] T. Sakai, A. Belyakov, R. Kaibyshev, H. Miura, J.J. Jonas, Dynamic and post-dynamic recrystallization under hot, cold and severe plastic deformation conditions, Prog Mater Sci 60 (2014) 130-207.

[38] F. Musin, A. Belyakov, R. Kaibyshev, Y. Motohashi, G. Itoh, K. Tsuzaki, MICROSTRUCTURE EVOLUTION IN A CAST 1421Al ALLOY DURING HOT EQUAL-CHANNEL ANGULAR EXTRUSION, Rev Adv Mater Sci 25(2) (2010) 107-112.

[39] A. Heidarzadeh, S. Mironov, R. Kaibyshev, G. Cam, A. Simar, A. Gerlich, F. Khodabakhshi, A. Mostafaei, D.P. Field, J.D. Robson, A. Deschamps, P.J. Withers, Friction stir welding/processing of metals and alloys: A comprehensive review on microstructural evolution, Prog Mater Sci 117 (2021).

Appendix A – supplementary figures

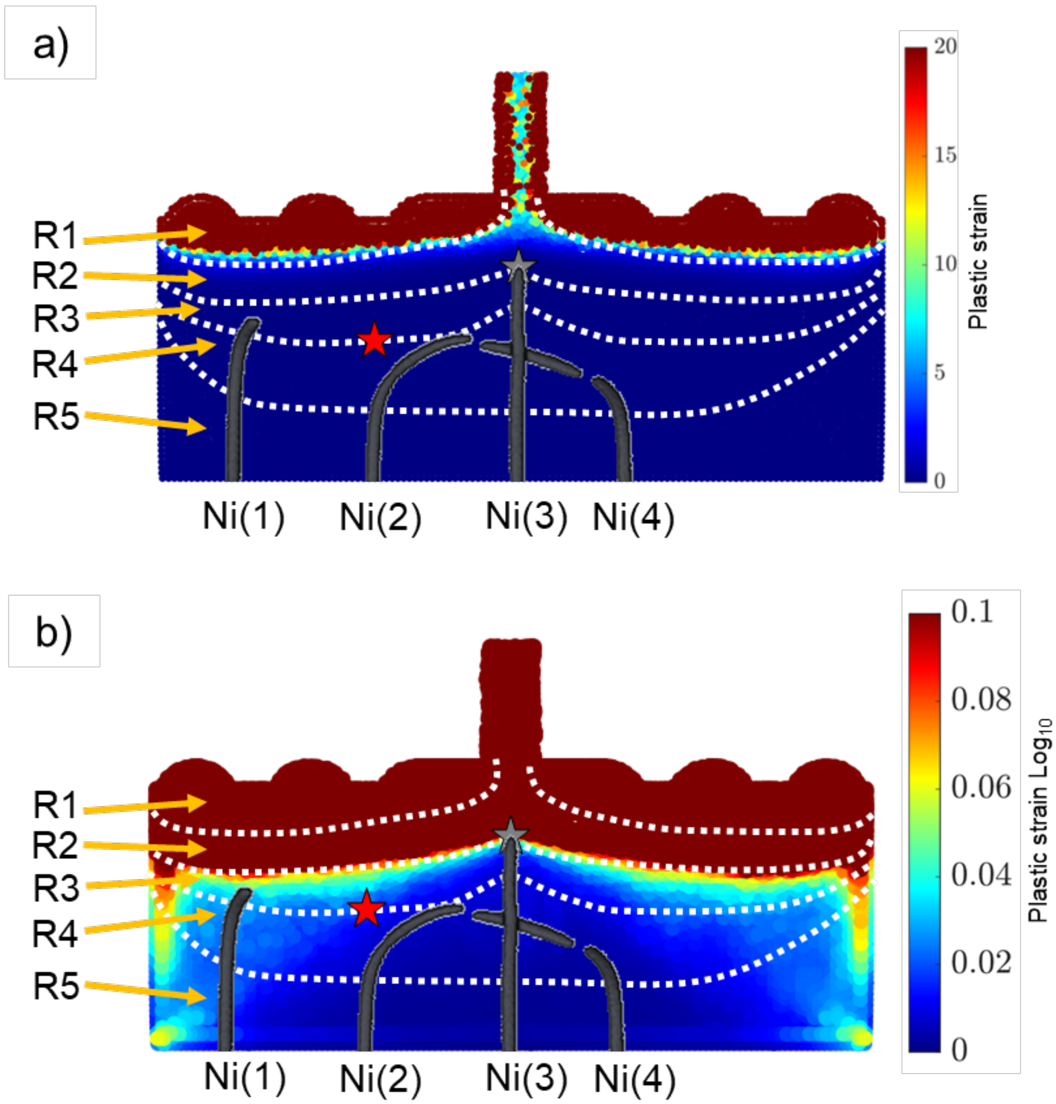

Figure S1. Smooth particle hydrodynamic simulation results highlighting the strain field after steady state friction extrusion at 150 RPM and feed rate of 8 mm.min-1: a) linear axis; b) logaritmic axis. The linear axis is useful to identify the core-shell microstructure forming due to the combination of high and low strain plastic flows, respectively.

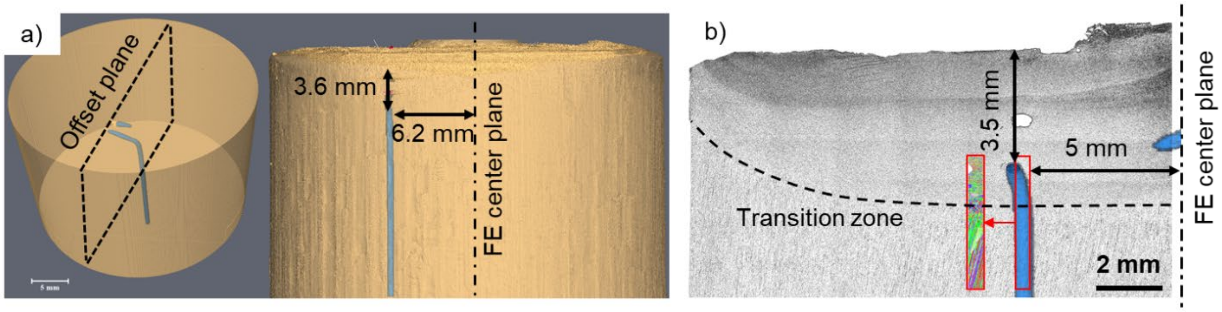

Figure S2. Location of the Al/Ni(5) thermoelectric junction fracture after interrupted friction extrusion at a die rotation speed of 150 RPM and feed rate of 8 mm.min-1: a) XCT scan analysis showing the position of the wire fracture and offset plane coordinates for targeted metallographic polishing; b) light optical microscopy image showing the exposed Al/Ni(5) thermoelectric fracture plane. The XCT scan results filtered for Ni are overlaid in b) to clarify the position of the region of interest.

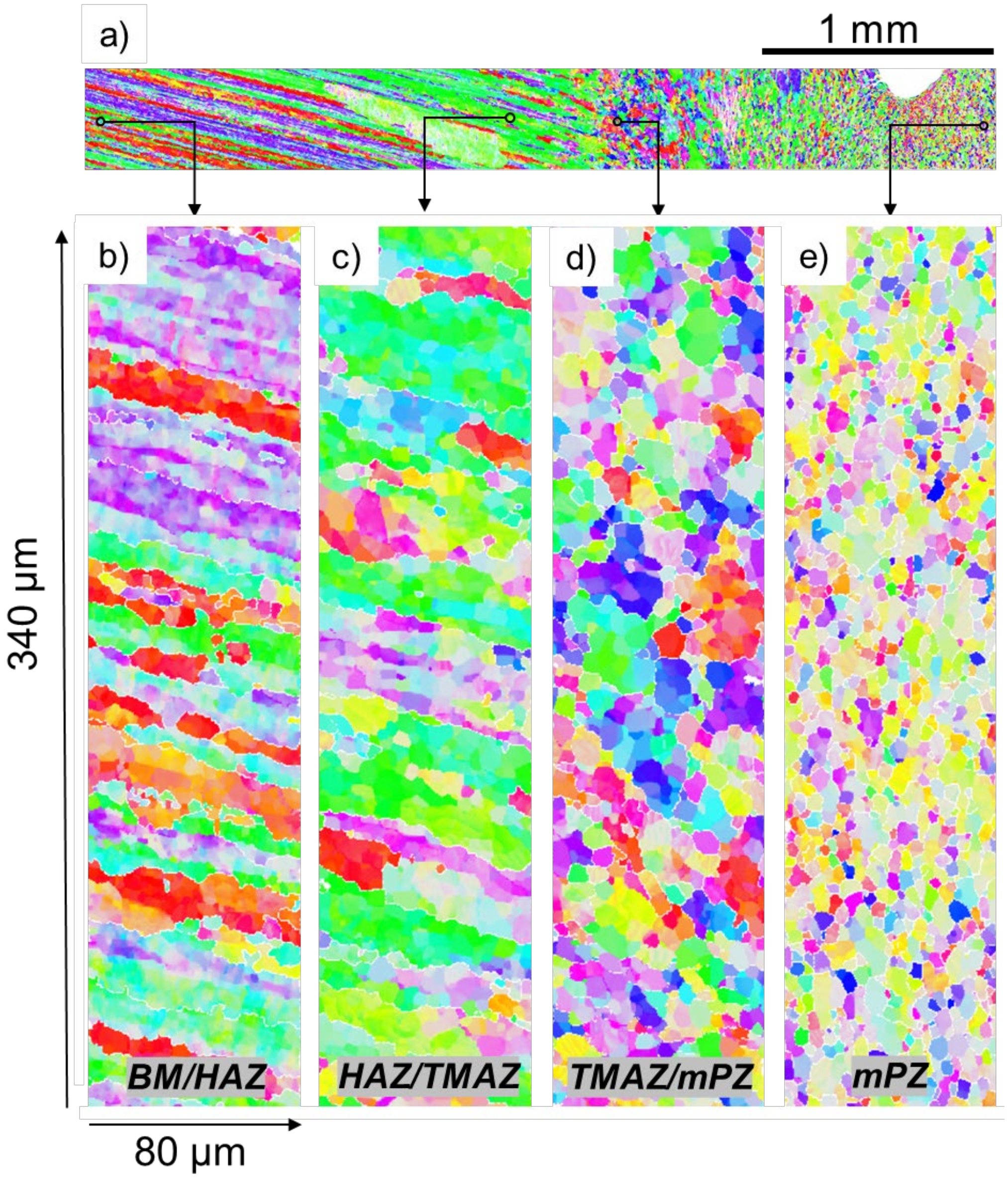

Figure S3. Detailed microstructure analysis via inverse pole figures in the Z direction after interrupted friction extrusion at 150 RPM and feed rate of 8 mm.min-1: a) large montage image of the microstructural transition from the base metal towards the mild processing zone; b), c), d), and e) show details of the BM, HAZ/TMAZ, TMAZ/mpZ, and mPZ regions, respectively.

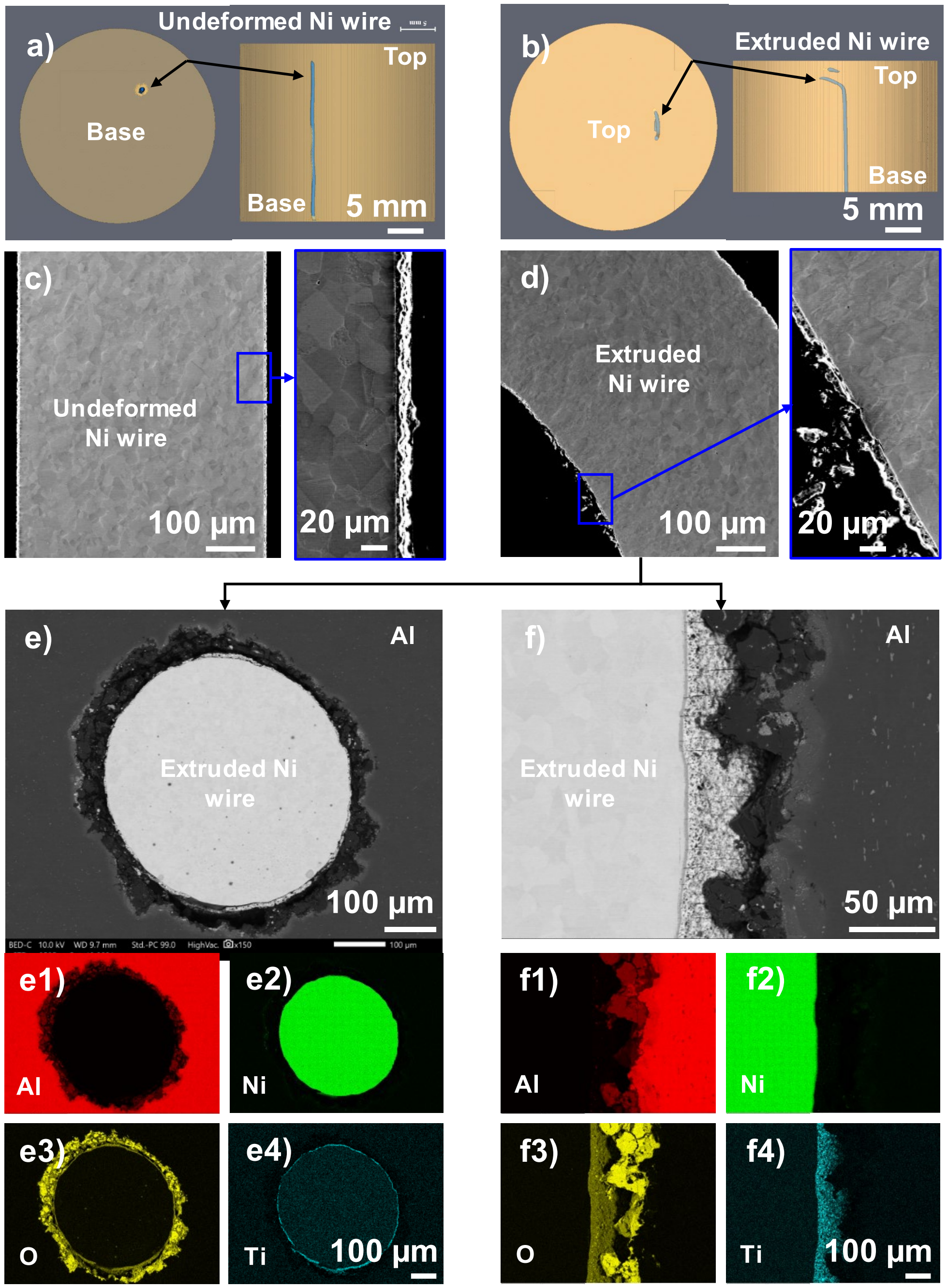

Figure S4. Microstructural and compositional characterization of the Ni wires before and after thermoelectric voltage measurements at 150 RPM and feed rate of 8 mm.min-1: a) and b) show XCT scan images from top and transverse section views for a single undeformed Ni wire before, and after interrupted friction extrusion, respectively; c) and d) show SEM images of the transverse section of undeformed and deformed Ni wires, respectively, highlighting the Ni/enamel/Al interfaces; e) and f) depict detailed images of the transverse and longitudinal sections of the Ni wire after interrupted friction extrusion; e1) to e4), and f1) to f4) show additional EDS compositional maps for Al (e1, f1), Ni (e2, f2), O (e3, f3) and Ti (e4, f4) of the enamel insulated Ni wires after friction extrusion. The formation of an additional interfacial oxide layer provides further electrical insulation during thermoelectric voltage measurements.

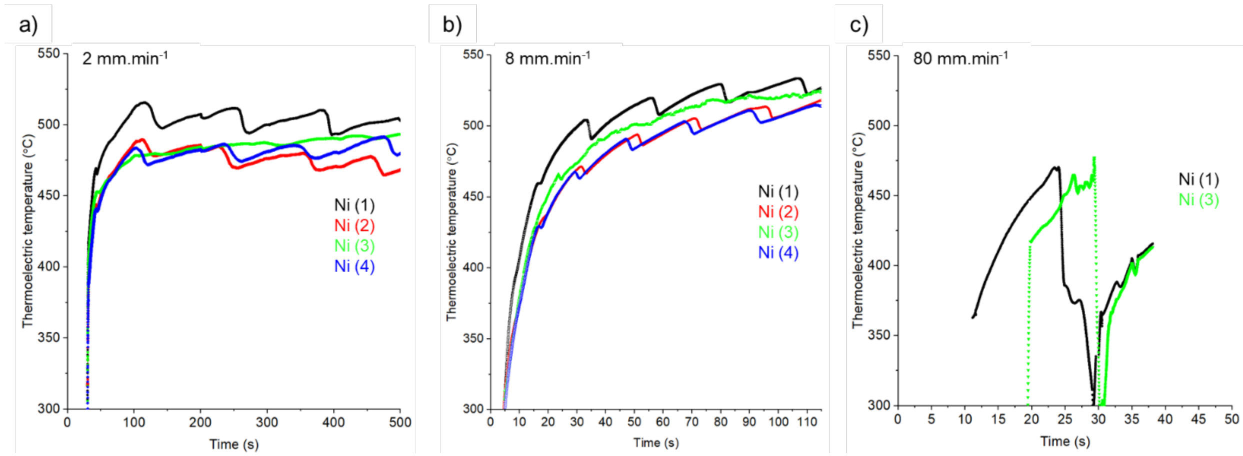

Figure S5. Thermoelectric temperature measurements along different radial positions during FE of instrumented Al 1100 billets: a) 150 RPM and 2 mm.min-1; b) 150 RPM and 8 mm.min-1; a) 150 RPM and 80 mm.min-1. The hottest part of the billet during internal measurements is related to the microstructure at the vicinity of the Ni(1) TE junction, which is near the outside diameter of the billet.

Pacific Northwest National Laboratory

902 Battelle Boulevard
P.O. Box 999
Richland, WA 99354

1-888-375-PNNL (7665)

www.pnnl.gov